INTERNATIONAL JOURNAL OF HYDROGEN ENERGY 42 (2017) 30691–30703

Available online at www.sciencedirect.com

ScienceDirect

journal homepage: www.elsevier.com/locate/he

Dendritic $Co_{0.52}Cu_{0.48}$ and $Ni_{0.19}Cu_{0.81}$ alloys as hydrogen generation catalysts via hydrolysis of ammonia borane

Wanlu Sang, Chenyang Wang, Xinghua Zhang, Xiaofei Yu, Chao Yu, Jianling Zhao, Xixin Wang, Xiaojing Yang, Lanlan Li***

School of Materials Science and Engineering, Hebei University of Technology, Tianjin, 300130, PR China

ARTICLE INFO

Article history:
Received 27 August 2017
Received in revised form
14 October 2017
Accepted 23 October 2017
Available online 20 November 2017

Keywords:
$Co_{0.52}Cu_{0.48}$ alloy
$Ni_{0.19}Cu_{0.81}$ alloy
Dendritic alloys
Ammonia borane
Hydrolysis

ABSTRACT

Dendritic Co–Cu and Ni–Cu alloys were employed as hydrogen generation catalysts via hydrolysis of ammonia borane (NH_3BH_3, AB). Dendritic $Co_{0.52}Cu_{0.48}$ and $Ni_{0.19}Cu_{0.81}$ alloys were successfully synthesized with starch by a facile and efficient in situ method at room temperature. The structure, morphology, and chemical composition of the as-obtained samples were characterized by X-ray diffraction (XRD), scanning electron microscopy (SEM) with energy dispersive X ray spectroscopy (EDX), transmission electron microscopy (TEM) inductively coupled plasma emission spectroscopy (ICP) and X-ray photoelectron spectroscopy (XPS). The characterization results revealed a dendritic and uniform distribution for the as-synthesized nanoparticles (NPs). Good performance towards the hydrolysis of AB was observed in all cases, although $Co_{0.52}Cu_{0.48}$ showed the highest hydrogen release rate (r, 2179 mL $min^{-1}\cdot g^{-1}$) and the lowest activation energy (E_a, 37.3 kJ mol^{-1}) among the samples prepared. The surface structure of the alloys and the reticular density of the different crystal faces were studied with the aim to explain the catalytic performance of the samples.

© 2017 Hydrogen Energy Publications LLC. Published by Elsevier Ltd. All rights reserved.

Introduction

Efficient production and storage of hydrogen have attracted attention worldwide owing to its potential to meet the increasing demand for efficient and clean energy from both economic and environmental points of view [1–4]. A large number of compounds with the potential to serve as hydrogen storage materials (e.g., metal hydrides, organic compounds, and ligand hydrides) have been developed [5,6]. Recently, significant attention has been paid to the generation of hydrogen from ammonia borane (BH_3NH_3, AB) since this compound possesses a high hydrogen content of 19.6 wt%, high stability, and a relatively low cost [7,8]. AB can be dehydrogenated by three different routes namely, thermal decomposition, alcoholysis, and hydrolysis. Hydrolysis is a convenient and widely used dehydrogenation method [9]. Previous reports have demonstrated that AB can release considerable amounts of hydrogen through hydrolysis at room temperature by using proper catalysts [10].

Effective dehydrogenation catalysts achieves high hydrogen release rates while also effectively suppressing the

* *Corresponding author.*
** *Corresponding author.*
E-mail addresses: yangxiaojing@hebut.edu.cn (X. Yang), Liabc@hebut.edu.cn (L. Li).
https://doi.org/10.1016/j.ijhydene.2017.10.130
0360-3199/© 2017 Hydrogen Energy Publications LLC. Published by Elsevier Ltd. All rights reserved.

reverse reaction. Various noble metals such as Au, Pt, Pd, Ru, Ag and Rh have been used in form of nanoparticles (NPs) as AB hydrolysis catalysts [11–14]. However, their high cost and limited resources largely hinder the development of practical applications which require efficient and low-cost catalysts with improved kinetic properties under moderate conditions. The utilization of more abundant transition metals (e.g., Fe, Co, Ni, and Cu, among others) for catalyzing the hydrolysis of

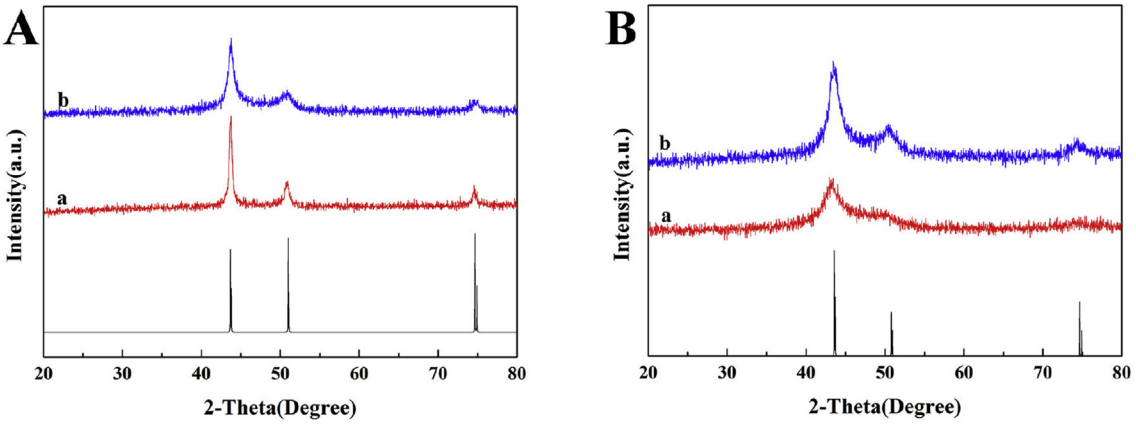

Fig. 1 – (A) XRD patterns of $Co_{0.52}Cu_{0.48}$ alloy catalysts prepared without (a) and with starch (b). (B) XRD patterns of $Ni_{0.19}Cu_{0.81}$ alloy catalysts prepared without (a) starch and with starch (b).

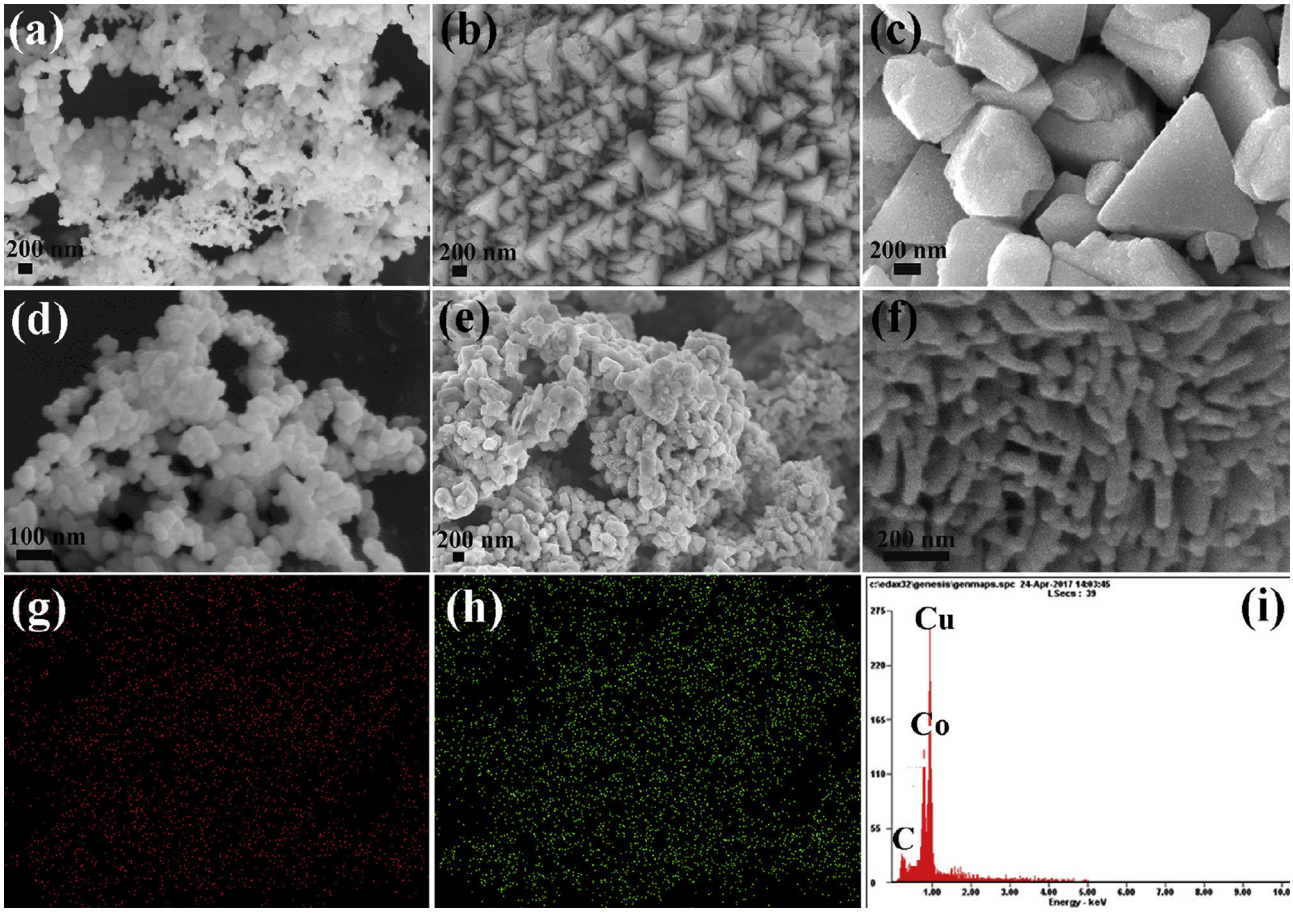

Fig. 2 – SEM images of: Co (a), Cu (b), $Co_{0.52}Cu_{0.48}$ alloy prepared without starch (c), Co (d), Cu (e), $Co_{0.52}Cu_{0.48}$ alloy prepared with starch (f), EDX mapping images of $Co_{0.52}Cu_{0.48}$ alloy prepared with starch samples (g and h), and EDX spectra of $Co_{0.52}Cu_{0.48}$ alloy prepared with starch samples (i).

AB with high efficiency has been recently explored. In this sense, Cu NPs have been widely used as AB hydrolysis catalysts [15–17]. In particular, divalent Cu has a standard reduction potential comparable to the valence of noble metals and can be readily reduced to zero valent Cu by a mild reducing agent such as diborane, making it an ideal AB hydrolysis catalyst. However, Cu possesses a moderate hydrolysis activity and is unstable under hydrolysis conditions [18]. Heterogeneous metal catalysts, despite showing superior catalytic performances than their monometallic counterparts, are highly prone to form agglomerates and present very high reactivity towards water and oxygen. Song et al. supported Co–Cu NPs on diamine-functionalized graphene, and this catalyst showed a remarkably enhanced performance towards the dehydrogenation of AB (i.e., turnover frequency (TOF) as high as 51.5 $mol \cdot H_2 \cdot mol \cdot catalyst^{-1} \cdot min^{-1}$) [19]. Lu prepared a Cu–Ni/MCM-41 catalyst by a simple liquid impregnation–reduction method with a TOF value towards the hydrolysis of AB of 15.0 $mol \cdot H_2 \cdot mol \cdot catalyst^{-1} \cdot min^{-1}$ [20]. The utilization of supports increases the cost and complicates the preparation of catalysts. Zhang et al. prepared porous hierarchical Cu@Ni cubic-cage microstructures by a one-step solvothermal reduction route, with the $Cu_{0.8}Ni_{0.2}$ catalyst releasing H_2 for 8 min with an apparent activation energy (E_a) of 40.53 kJ mol^{-1} [21]. Wang et al. prepared novel Cu@CoNi trimetallic core–shell NP catalysts with maximum hydrogen generation rate (r) and E_a of 7340.80 mL $min^{-1} \cdot g^{-1}$ and 36.08 kJ mol^{-1}, respectively [22]. Cu@Ni showed a cubic-cage

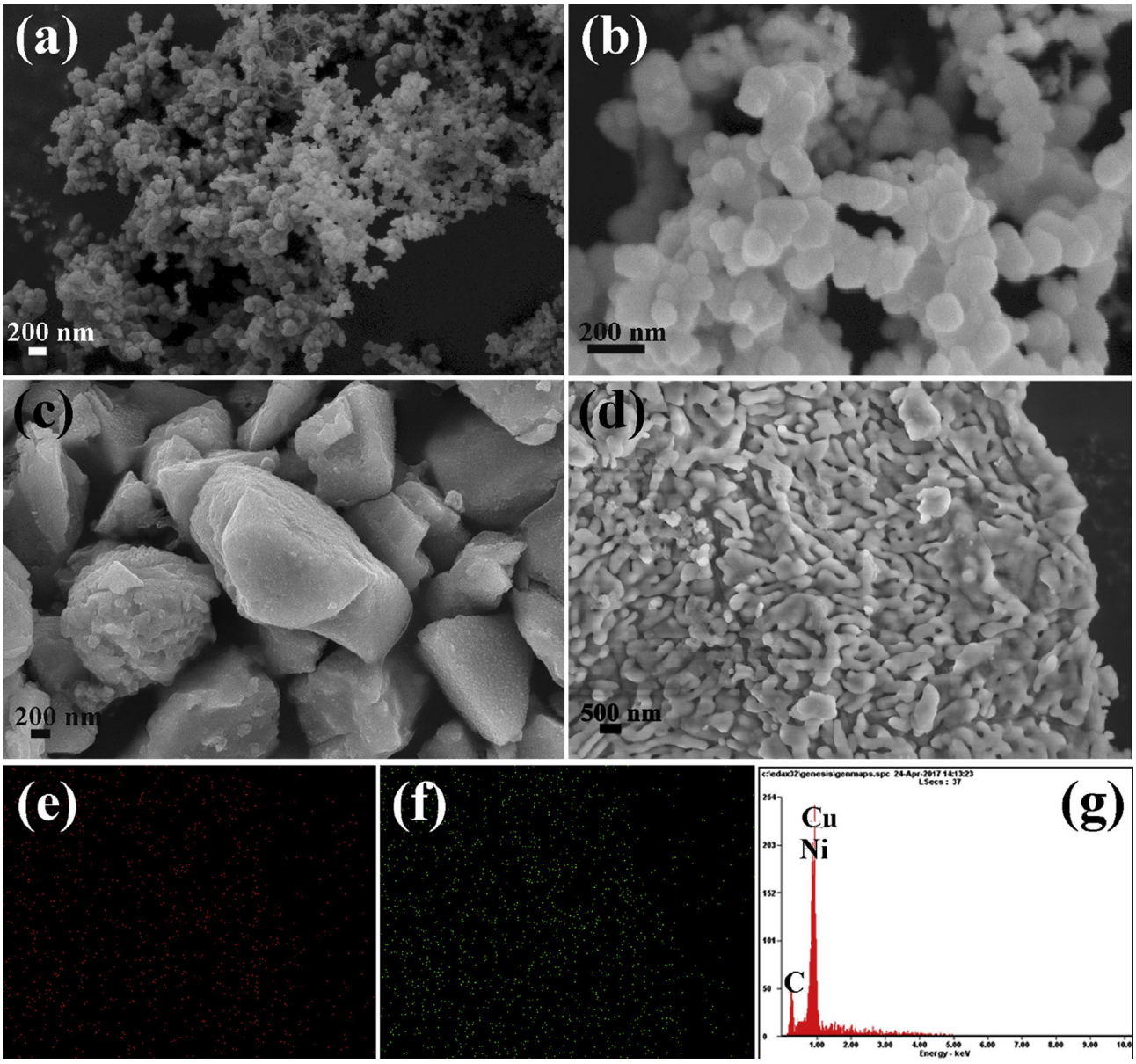

Fig. 3 – SEM images of Ni prepared without starch (a), Ni prepared with starch (b), $Ni_{0.19}Cu_{0.81}$ alloy prepared without starch (c), $Ni_{0.19}Cu_{0.81}$ alloy prepared with starch(d), EDX mapping images of $Ni_{0.19}Cu_{0.81}$ alloy prepared with starch samples ((e) and (f)), and EDX spectra of $Ni_{0.19}Cu_{0.81}$ alloy prepared with starch samples (g).

shape with small NPs while Cu@CoNi was composed of trimetallic core-shell NPs with excellent catalytic performance. It can be concluded that the morphology of the material plays a key role in determining its catalytic performance. Therefore, changing the morphology of the catalysts and, more particularly, downsizing the NPs to a uniform size distribution, helps improve their catalytic activities.

A general solution to stabilize or protect the metallic nanoparticles is to coat them with some outer materials including precious metals, silica, polymeric hydrogel, microgel, carbon, capsule and also polymers. Herein, we employed soluble starch as both dispersing and air resistance coating agents for synthetizing aqueous solutions of Co–Cu and Ni–Cu alloy heterogeneous catalysts at room temperature and in an easy manner. Soluble starch, the main energy reserve of plants, can form water dispersions [23], thereby avoiding the utilization of volatile organic solvents, expensive organometallic precursors, and synthetic macromolecules. This is of pivotal importance from "green" synthetic strategy and industrial scale manufacture perspectives. In this work, starch binds gently to inner NPs forming dendritic morphologies constituted by NPs of ca. 5 nm in size. The synthesized Co–Cu and Ni–Cu alloy heterogeneous NPs possessed high catalytic activity towards the hydrolysis of AB for chemical storage of hydrogen at room temperature.

Experimental

Chemicals

AB, cobalt chloride hexahydrate ($CoCl_2 \cdot 6H_2O$), nickel chloride hexahydrate ($NiCl_2 \cdot 6H_2O$), copper chloride hexahydrate ($CuCl_2 \cdot 2H_2O$), sodium borohydride ($NaBH_4$), sodium hydroxide (NaOH), and starch were used as received.

Catalysts preparation

Preparation of the starch solution: Starch powder was added to deionized water and the resulting solution was heated to 368 K for 15 min in an oil bath. The clear solution obtained was subsequently cooled down to room temperature for its use.

Single metal (Co, Ni, and Cu) and alloy ($Co_{0.52}Cu_{0.48}$ and $Ni_{0.19}Cu_{0.81}$) NPs with and without starch were synthesized by an in situ method. 5.94 mg of $CoCl_2 \cdot 6H_2O$ (or $NiCl_2 \cdot 6H_2O$) and 23.76 mg of $CuCl_2 \cdot 2H_2O$ were ultrasonically mixed with the as-prepared starch solution (or deionized water) under an Ar atmosphere for 10 min at room temperature. Subsequently, 1.2 mg of NaOH, 3 mg of $NaBH_4$, and 20 mg of NH_3BH_3 were simultaneously added. For comparison, Co, Ni, and Cu NPs were also synthesized in the presence of surfactant or deionized water under similar conditions. The as-prepared catalyst is easy to be oxidized, so argon is used as a protective gas. $NaBH_4$ is a reducing agent. NaOH is added to inhibit the release of hydrogen from $NaBH_4$ which may increase the total H_2 volume released from NH_3BH_3 according to previous work [24]. In this experiment, the addition of NH_3BH_3 and $NaBH_4$ is in the same time. The in-situ synthesis was used in order to prevent the as-synthesized production to be oxidized [25].

Catalysts characterization

The as-synthesized catalysts were characterized by powder X-ray diffraction (XRD, Rigaku D/max-2500 X-ray generator, Cu Ka radiation), scanning electron microscopy coupled with energy dispersive X-ray spectroscopy (SEM-EDX, JEOL JSM-6700F), transmission electron microscopy (TEM, Philips Tecnai F20, 200 kV), inductively coupled plasma emission spectroscopy (ICP) and X-ray photoelectron spectroscopy (XPS, ESCALAB 250Xi).

Hydrogen generation measurements

The hydrogen generation rate (r) via hydrolysis was measured in order to evaluate the activity of the catalysts. r can be determined from the slopes of the fitting lines derived from the curves of the generated hydrogen volumes (measured below 60 mL) versus the reaction time: $r_{(mL \cdot min^{-1} \cdot g^{-1})} = V_{(generated\ H2,mL)}/(t_{(time,\ min)} \times m_{(amount\ of\ the\ catalyst,\ g)})$ [26]. All reductants were placed in a three-necked flask, which was subsequently immersed in a constant temperature bath with controlled temperature. The reaction was performed without stirring to prevent the catalyst from being stuck to the magnetic stirrer. A small power ultrasonic cleaner was used during the reaction to provide uniform mixture of the reactants. The outlet exhaust of the flask was connected to a micro-gas flowmeter (RTK-GMA-II) to monitor the evolved H_2 volume. r was determined at different temperatures while keeping the total hydrogen volume below 60 mL for obtaining the apparent E_a [27]. Based on the slope of the Arrhenius plot, E_a was calculated according to the equation: $\ln k = \ln A - E_a/RT$ [28] where the rate constant $k_{(mol \cdot min^{-1} \cdot g^{-1})}$ was obtained as: $k_{(mL \cdot min^{-1} \cdot g^{-1})} = (P_{(Pa)} \times r_{(mL \cdot min^{-1} \cdot g^{-1})})/(8.314 \times T_{(K)})$ with the ideal-gas state equation at ambient atmosphere.

Results and discussion

Catalyst characterization

The $Co_{0.52}Cu_{0.48}$ and $Ni_{0.19}Cu_{0.81}$ alloy catalysts were prepared by an in situ method [29]. Co^{2+}, Ni^{2+}, and Cu^{2+} were simultaneously reduced to alloy NPs during the reduction process owing to the strong reducing properties of $NaBH_4$.

The XRD patterns of the $Co_{0.52}Cu_{0.48}$ and $Ni_{0.19}Cu_{0.81}$ alloys prepared with and without starch are shown in Fig. 1(a) and (b). Noticeably, both prepared with and without starch alloys showed similar XRD patterns. Diffraction peaks centered at ca. $2\theta = 43.7$, 51.1, and 74.8° were observed for both alloys and respectively ascribed to the (111), (200), and (220) crystal planes of face-centered cubic (fcc) $Co_{0.52}Cu_{0.48}$ (JCPDS No. 50–1452) and $Ni_{0.19}Cu_{0.81}$ (JCPDS No. 47–1406) phases. No additional were observed, thereby revealing the high purity of the $Co_{0.52}Cu_{0.48}$ and $Ni_{0.19}Cu_{0.81}$ samples. The samples prepared with starch showed lower particle sizes than their deionized water-prepared counterparts, as revealed by the broader XRD peaks of the formers. When the ratios of metal element changed during preparation, the XRD patterns performed similarity.

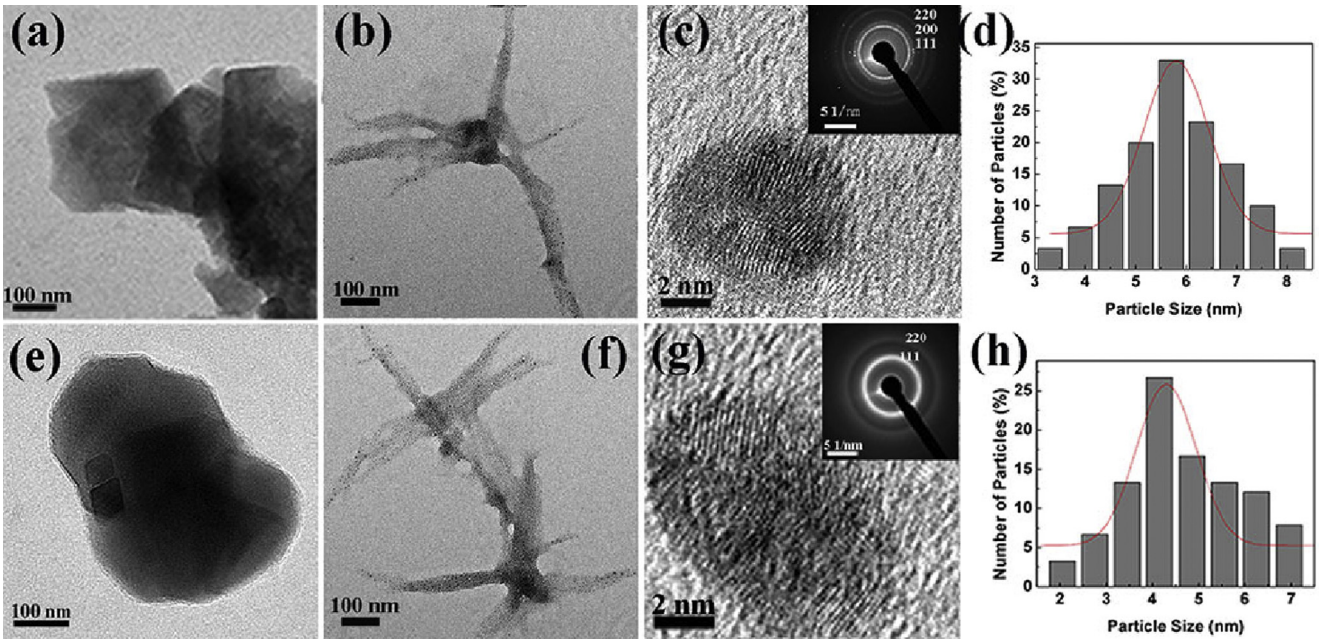

Fig. 4 – TEM images of $Co_{0.52}Cu_{0.48}$ alloy prepared without starch (a), $Ni_{0.19}Cu_{0.81}$ alloy prepared without starch (e),$Co_{0.52}Cu_{0.48}$ alloy prepared with starch (b) and $Ni_{0.19}Cu_{0.81}$ alloy prepared with starch (f), HRTEM image and the selected area electron diffraction pattern of $Co_{0.52}Cu_{0.48}$ alloy prepared with starch (c) and $Ni_{0.19}Cu_{0.81}$ alloy prepared with starch (g), size distributions for $Co_{0.52}Cu_{0.48}$ alloy prepared with starch (d) and $Ni_{0.19}Cu_{0.81}$ alloy prepared with starch (h).

Fig. 2 shows the SEM images of the Co, Cu, and $Co_{0.52}Cu_{0.48}$ catalysts prepared with and without starch. As clearly shown in Fig. 2, the samples prepared with and without starch showed significantly different morphologies. Thus, when compared to the starch-prepared samples (Fig. 2d–f), the catalysts prepared with deionized water (Fig. 2a–c) showed larger and more irregular particles. Addition of starch resulted in samples with different morphologies comprised of small granules (Fig. 2d–f). Thus, in the case of the $Co_{0.52}Cu_{0.48}$ alloy (Fig. 2f), addition of starch favored the transformation of large size irregular blocks into a uniform dendritic microstructure morphology with a length of 200–500 nm. In order to confirm the composition of the alloys, EDX mapping (Red: Co, Green: Cu) was carried out on the $Co_{0.52}Cu_{0.48}$ alloy prepared with starch (Fig. 2g and h). The EDX spectrum (Fig. 2i) confirmed the elemental compositions of the alloys.

Fig. 3 shows the SEM images of the Ni and $Ni_{0.19}Cu_{0.81}$ alloy catalysts prepared with and without starch. The catalysts synthetized in the absence of starch were comprised of larger and irregular particles with a size of 0.2–0.5 μm (Fig. 3a and c). In contrast, the samples prepared with starch were comprised of spherical particles with lower size (0.07–0.1 μm, Fig. 3b). The $Ni_{0.19}Cu_{0.81}$ alloy showed a coral-like dendritic structure (Fig. 3d). In order to determine the elemental composition and distribution of the alloys, the EDX spectrum and elemental mapping of $Ni_{0.19}Cu_{0.81}$ was determined (Fig. 3e–g). As shown in the EDX spectrum (Fig. 3g), the alloy was mainly formed by metallic Cu and Ni. The elemental mapping (Ni: red, Cu: green, Fig. 3e and f) revealed that both Cu and Ni elements were uniformly distributed, thereby suggesting the formation of an alloy, in line with the XRD results.

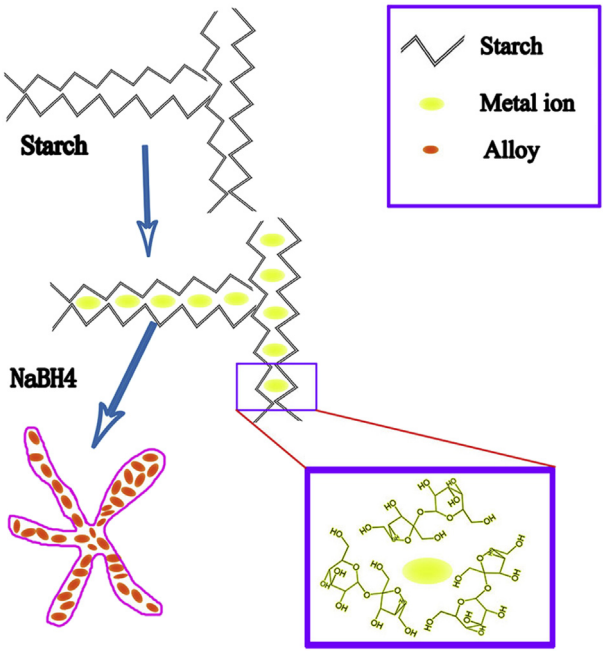

Fig. 5 – The proposed formation process for dendritic alloy nanocatalysts. The "egg-box" model is represented by yellow circles depicting metal cations positioned between starch. (For interpretation of the references to colour in this figure legend, the reader is referred to the web version of this article.)

TEM was employed to further observe the microstructure of the dendritic alloys. Fig. 4 show typical TEM images of the as-obtained $Co_{0.52}Cu_{0.48}$ and $Ni_{0.19}Cu_{0.81}$ alloy samples prepared without starch (Fig. 4a and e) and with starch (Fig. 4b and f), respectively. The dendritic alloy starch-prepared catalysts showed particles lower in size and more uniformly distributed than their deionized water-prepared counterparts. Catalyst without starch is agglomerated seriously about 400 nm (Fig. 4a and e). From the size distribution histograms (Fig. 4d and h), catalysts with starch are well distributed with an average diameter of about 5 nm. Thus, the particle size significantly decreased for the starch-prepared samples as compared to the deionized water-prepared counterparts (average diameter: 5 nm versus 400 nm). Clear lattice fringes were observed in the high-resolution TEM (HRTEM) images and the selected area electron diffraction (SEAD) patterns are shown in Fig. 4c and g, the indexes of the lattice planes were marked in the images.

Based on the above observations, starch has two important functions during the formation of dendritic alloy nanocatalysts. First, starch favored the dispersion of metal ions, preventing agglomeration and oxidization during the formation of the alloy. Thus, starch can strongly bind multi-valent cations through its functional groups making use of its buckled chain (i.e., a two-dimensional analogue of a "egg-box" [30], Fig. 5) with interstices in which the cations may be packed and coordinated, such that each cation is surrounded by starch. In our reaction system, the initial nucleation of the alloy was constrained to NPs by starch. Second, starch facilitated the formation of dendritic alloy nanocatalysts. Thus, the steric hindrance of starch and the air permeation of the cationic starch system at the initial stage prevented NPs aggregation, thereby allowing the formation of dendritic alloy nanocatalysts after addition of $NaBH_4$ (Fig. 5). During the reaction, some starch chains are connected to form a dendritic structure.

With the aim to determine the composition and oxidation state of the alloys, it is necessary to carry out surface elemental analysis by XPS. The XPS spectra along with the peak resolving and fitting results for the $Co_{0.52}Cu_{0.48}$ and $Ni_{0.19}Cu_{0.81}$ alloys prepared with starch are displayed in Fig. 6. For the peak differentiating and imitating (PDI) treatment, the binding energy was corrected by taking the C1s peak of contaminant carbon as a reference (284.5 eV). The main absorptions corresponded to Co2p, Ni2p, and Cu2p transitions. As shown in Fig. 6a, the high-resolution XPS Co2p spectrum was comprised of two peaks at 780.8 and 796.9 eV ascribed to Co (0) 2p3/2 and Co(0)2p1/2 transitions, respectively. Nevertheless, two additional peaks were observed at slightly higher binding energies, thereby revealing the existence of oxidized Co. The small particle size of the $Co_{0.52}Cu_{0.48}$ alloy NPs could have facilitated the oxidation of Co(0). The deconvolution of

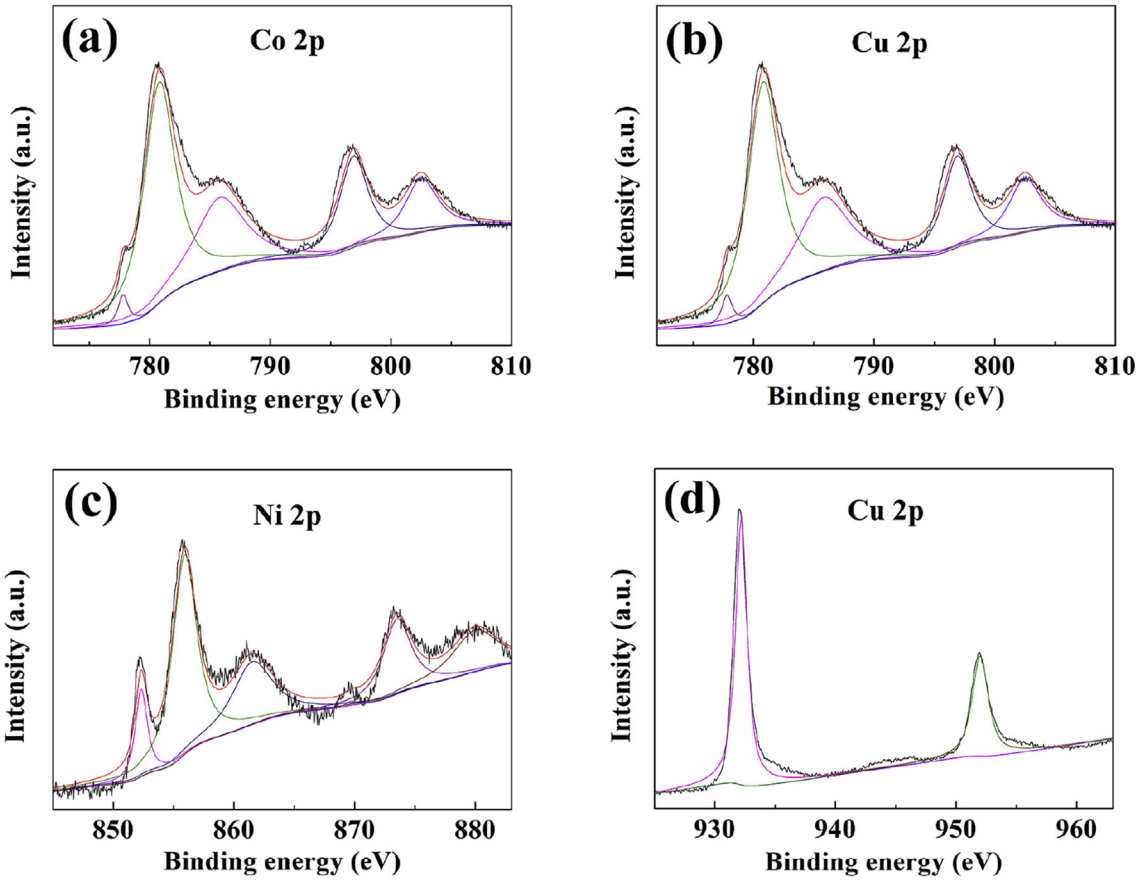

Fig. 6 – XPS spectra of $Co_{0.52}Cu_{0.48}$ alloy perpared with starch: Co2p (a) and Cu2p (b); XPS spectra of $Ni_{0.19}Cu_{0.81}$ alloy perpared with starch: Ni2p (c) and Cu2p (d).

the Cu2p spectrum (Fig. 6b) revealed peaks at 932.2 and 954.5 eV ascribed to the Cu(0)2p2/3 and Cu(0)2p1/2 transitions, respectively, while the three additional peaks were assigned to oxidized Cu. The PDI results for the Ni2p band (Fig. 6c) revealed two peaks at 852.3 and 869.7 eV which corresponded to Ni(0)2p3/2 and Ni(0)2p1/2 transitions, respectively. Two additional peaks were observed at a slightly higher binding energy, thereby revealing the existence of nickel oxidized species. The small size of the $Ni_{0.19}Cu_{0.81}$ alloy NPs could have facilitated the oxidation of Ni(0). Analogously, the measured binding energies of the Cu2p3/2 and 2p1/2 bands (933.2 and 954.5 eV, respectively) were slightly lower than the standard values corresponding to Cu(0) (932.6 and 955.2 eV). The existence of cobalt oxide and copper oxide species, confirmed by the XPS measurements, was likely produced via air exposure during XPS sampling. We tested the catalytic activities by in

Table 1 – The ratios of Ni/Cu for Ni_xCu_{1-x} and Co/Cu for Co_xCu_{1-x} tested by ICP.

Samples	$Co_{0.25}Cu_{0.75}$	$Co_{0.5}Cu_{0.5}$	$Co_{0.75}Cu_{0.25}$	$Ni_{0.25}Cu_{0.75}$	$Ni_{0.5}Cu_{0.5}$	$Ni_{0.75}Cu_{0.25}$
Co/Cu (ppm)	44.94:141.38	132.51:146.22	81.42:22.46	–	–	–
Co/Cu (at%)	0.25:0.75	0.50:0.50	0.80:0.20	–	–	–
Ni/Cu (ppm)	–	–	–	44.06:145.05	43.46:54.08	125.33:77.79
Ni/Cu (at%)	–	–	–	0.17:0.83	0.47:0.53	0.64:0.36

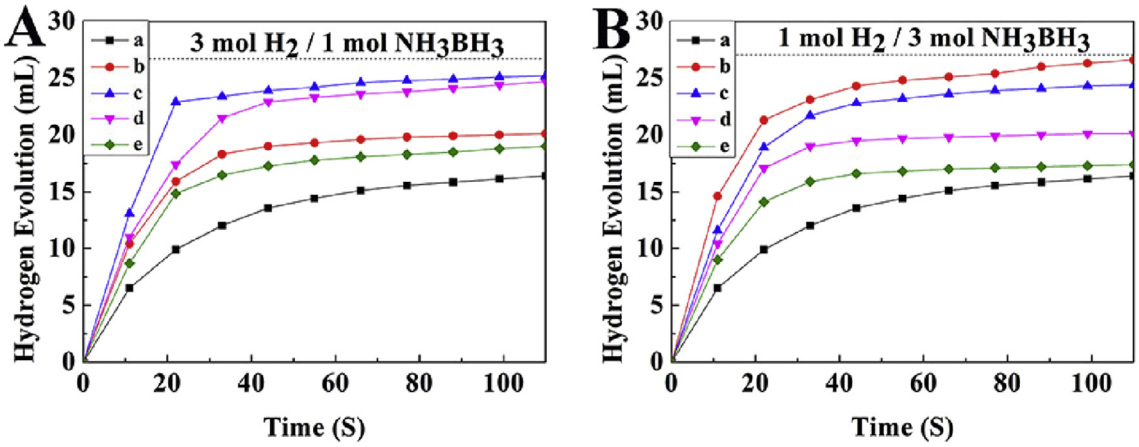

Fig. 7 – Hydrogen generation from AB (0.5 wt %, 10 mL) containing as-prepared catalysts (29.7 mg) prepared with starch at 25 °C. (A) Co_xCu_{1-x} NPs: (a) $x = 0$ (b) $x = 0.25$ (c) $x = 0.5$ (d) $x = 0.75$ (e) $x = 1$.(B) Ni_xCu_{1-x} NPs: (a) $x = 0$ (b) $x = 0.25$ (c) $x = 0.5$ (d) $x = 0.75$ (e) $x = 1$.

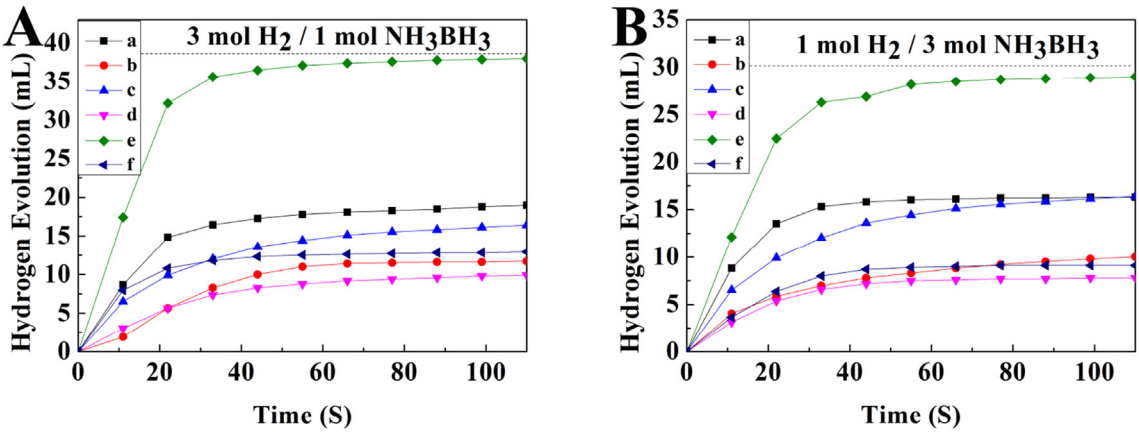

Fig. 8 – Hydrogen generation from AB (0.5 wt %, 10 mL) containing as-prepared catalysts (29.7 mg) at 25 °C. (A): Co_xCu_{1-x} catalysts (a) Co prepared with starch; (b) Co prepared without starch; (c) Cu prepared with starch; (d) Cu prepared without starch; (e) $Co_{0.52}Cu_{0.48}$ alloy prepared with starch; (f) $Co_{0.52}Cu_{0.48}$ alloy prepared with starch; (B): $Ni_{0.19}Cu_{0.81}$ catalysts (a) Ni prepared with starch; (b) Ni prepared without starch; (c) Cu prepared with starch; (d) Cu prepared without starch; (e) $Ni_{0.19}Cu_{0.81}$ alloy prepared with starch; (f) $Ni_{0.19}Cu_{0.81}$ alloy prepared with starch.

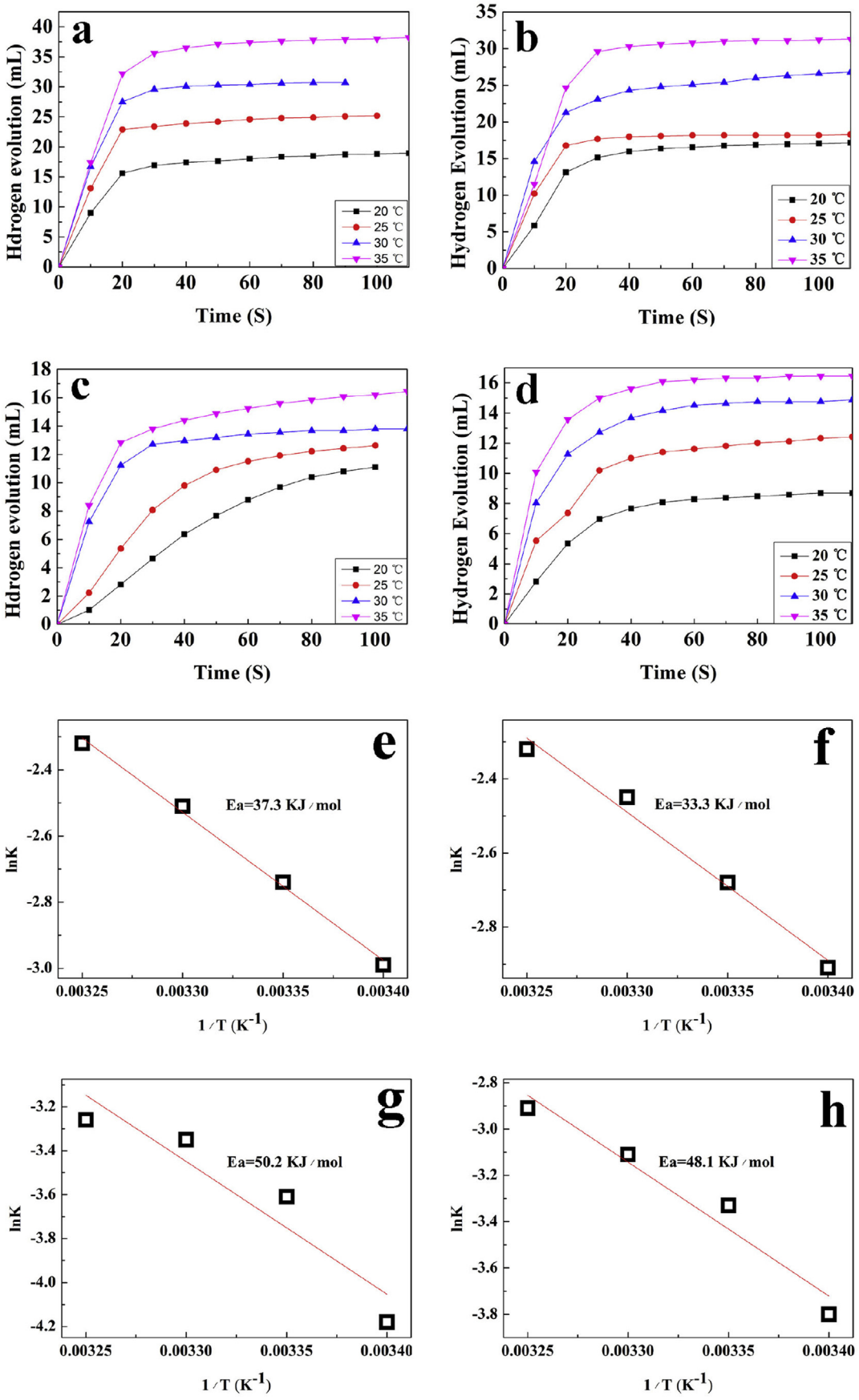

Fig. 9 – Temperature effect on hydrogen generation rate using 29.7 mg catalysts in AB solution (0.5 wt %, 10 mL): (a) $Co_{0.52}Cu_{0.48}$ alloy prepared with starch; (b) $Ni_{0.19}Cu_{0.81}$ alloy prepared with starch; (c) $Co_{0.52}Cu_{0.48}$ alloy prepared without

situ method. So it was not oxidized when the catalyst catalyzed the hydrolysis of AB.

Co_xCu_{1-x} and Ni_xCu_{1-x} alloys ($x = 0$, 0.25, 0.5, 0.75 and 1, x stands for the raw material ratio) were prepared by changing the Cu ratio during the preparation. In order to determine the ratio of the two metal content in the catalyst, we detected the elemental ratios of the samples by ICP, which are summarized in Table 1. When $x = 0.5$ for Co_xCu_{1-x}, the ICP results agree well with that of XRD. The element ratios agree well for $Ni_{0.19}Cu_{0.81}$ so as to Ni_xCu_{1-x}.

Catalytic activities

The catalytic activities of the synthesized catalysts was investigated for hydrolysis of AB. Fig. 7 shows the generated H_2 amount as a function of time with 29.7 mg of catalysts prepared with starch at 25 °C. In Fig. 7A and B, the single metal nanoparticles exhibit weak catalytic activity, while the release of hydrogen is greatly quickened in the presence of bimetallic nanoparticles during the hydrolysis of AB. The activities of the catalysts with different metal contents vary with the elemental composition. In Fig. 7A, as the Co content increases, the hydrogen release rates first increase and then decrease, showing a volcano-shape trend. When the raw material ratio of Co content reaches 50%, which is $Co_{0.52}Cu_{0.48}$ detected by XRD and ICP testing, the catalytic activity is the best. In Fig. 7B, as the ratio of Ni increases, the hydrogen release rates show similar tendency as Co_xCu_{1-x}. When the raw material ratio of Ni content is 25%, that is $Ni_{0.19}Cu_{0.81}$ confirmed by XRD and ICP results, the catalyst show the best effect.

The hydrogen generation catalytic activities via AB hydrolysis of the synthesized $Co_{0.52}Cu_{0.48}$ and $Ni_{0.19}Cu_{0.81}$ alloy catalysts prepared with and without starch were compared with those of single metal Co, Ni, and Cu catalysts. Fig. 8 shows the amount of hydrogen generated from a 10 mL AB solution containing 29.7 mg of catalysts as a function of time. While the NPs synthesized without starch exhibited low catalytic activity towards the hydrolysis of AB, the amount of released hydrogen significantly increased in the presence of samples prepared with starch, as an indicative of their high catalytic activities. The $Co_{0.52}Cu_{0.48}$ and $Ni_{0.19}Cu_{0.81}$ alloys synthesized with starch showed high catalytic activities. Thus, when contacted with these samples, the AB solution was completely hydrolyzed in only 1 min, thereby revealing the higher r values of the starch-prepared alloys. Once the hydrogen release reaction was finished, the hydrogen to initial AB molar ratio was calculated, and a value close to 3.0 was obtained. The $Co_{0.52}Cu_{0.48}$ alloy prepared with starch showed the best catalytic performance among the samples studied herein, with a r of nearly 2179 mL $min^{-1}\cdot g^{-1}$ (versus 2066 mL $min^{-1}\cdot g^{-1}$ for the $Ni_{0.19}Cu_{0.81}$ alloy prepared with starch). These values were larger than those of Pt_3Co (ca. 1380 mL $min^{-1}\cdot g^{-1}$) and Pt_3Ni (ca. 1388 mL $min^{-1}\cdot g^{-1}$) alloy catalysts reported by Yang et al. [31].

This outstanding catalytic performance can be explained by the above XPS results. Thus, the catalytic activity trend coincides with the absolute variation of the Cu2p3/2 binding energy in the alloy samples. In theory, a higher Cu content in the alloy should facilitate the transfer of electric charges from Cu to Ni or Co, thereby increasing the number of active sites on the surface of the catalysts. The higher catalytic activities of bimetallic catalysts as compared to single metals has been previously reported. Li [32] and Yamada [33] separately reported that the Cu content can largely influence the catalytic activities of Cu-based bimetallic catalyst.

Fig. 9a–d shows the effect of temperature on the r values of the alloy catalysts. As expected, the r values increased dramatically with temperature. The total volumes of hydrogen generated via hydrolysis of AB slightly increased with temperature. The r values at various temperatures are summarized in Table 2, while Fig. 9e–h shows the Arrhenius plots (lnk versus the reciprocal absolute temperature (1/T)) for different catalysts. According to the slopes of the straight sections, apparent E_a values of 37.3 and 33.3 kJ mol^{-1} were respectively obtained for the $Co_{0.52}Cu_{0.48}$ and $Cu_{0.81}Co_{0.19}$ alloy catalysts prepared with starch (versus 50.2 and 48.05 kJ mol^{-1} for their respective deionized water-prepared counterparts).

The cycling capability and durability are very important for the practical application of a catalyst within a hydrogen generation system. The prepared catalysts can be facilely and efficiently reused by simply being rinsed with distilled water without complicate post-treatment process. The recyclablity of $Co_{0.52}Cu_{0.48}$ and $Ni_{0.19}Cu_{0.81}$ alloy catalysts up to fifth run for hydrolysis of AB are shown in Fig. 10. The cycling performance of the catalytic rate decreased with the number of cycles. $Co_{0.52}Cu_{0.48}$ retained 66% and $Ni_{0.19}Cu_{0.81}$ retained 61% of its initial catalytic activity toward the hydrolysis of AB after 5 cycles, thereby demonstrating a favorable catalytic stability. This value was larger than that of Ag@CoFe/graphene (ca. 59% after 5 cycles) reported by Yang et al. [34], and also significantly higher than that of $Co_{0.9}Ni_{0.1}$/graphene (ca. 44% after 5 cycles) [35].

The catalytic performance of several different catalysts was compared in table Table 3. Our TOF (turn over frequency) value (2.7–3.4 mol $H_2\cdot mol^{-1}$ Catalyst$\cdot min^{-1}$) is lower than that of some other catalyst (2.8–339.5 mol $H_2\cdot mol^{-1}$ Catalyst$\cdot min^{-1}$). However, the other catalysts listed in Table 3 have supporters which made the preparation complex and precious metals (e.g., Ru, Rh) which increase the cost of hydrogen release. Our catalysts are simple to prepare with low-cost transition metal. Comparing the E_a values of different catalysts, the E_a values of the catalysts we prepared (33.7 and 33.3 kJ mol^{-1}) were relatively low. $Co_{0.52}Cu_{0.48}$ retained 66% and $Ni_{0.19}Cu_{0.81}$ retained 61% of its initial catalytic activity toward the hydrolysis of AB after 5 cycles. Although the TOF values herein obtained were lower than some of other alloy catalysts, $Co_{0.52}Cu_{0.48}$ and $Ni_{0.19}Cu_{0.81}$ showed promising cycle performance.

The above results indicated that the synthesized alloy catalysts show superior performance towards the hydrolysis

starch; (d) $Ni_{0.19}Cu_{0.81}$ alloy prepared without starch. Arrhenius plots of lnk vs the reciprocal absolute temperature 1/T in the temperature range of 20–35 °C: (e) $Co_{0.52}Cu_{0.48}$ alloy prepared with starch; (f) $Ni_{0.19}Cu_{0.81}$ alloy prepared with starch; (g) $Co_{0.52}Cu_{0.48}$ alloy prepared without starch; (h) $Ni_{0.19}Cu_{0.81}$ alloy prepared without starch.

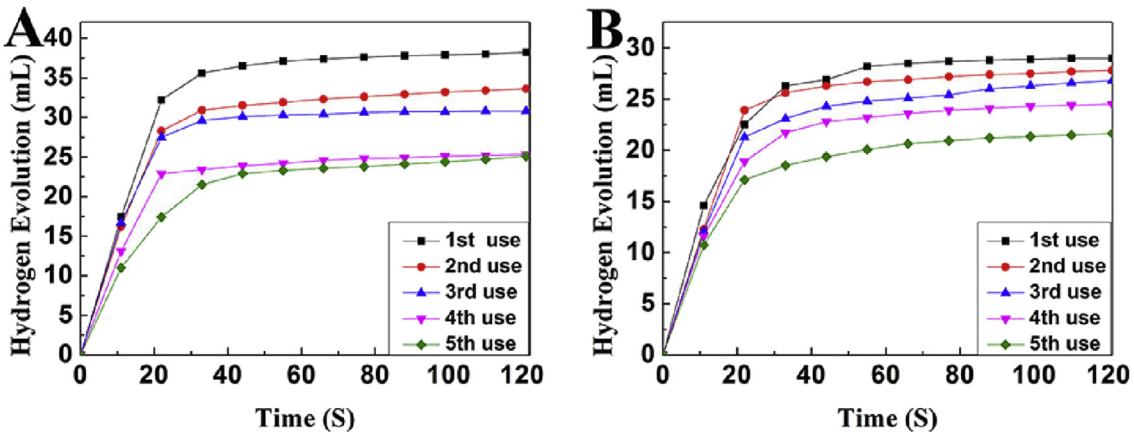

Fig. 10 – Cycling ability of the prepared catalyst: (A) $Co_{0.52}Cu_{0.48}$; (B) $Ni_{0.19}Cu_{0.81}$.

of AB than pure Cu, Co, and Ni metals. Additionally, $Co_{0.52}Cu_{0.48}$ alloy NPs prepared with starch exhibited the highest catalytic activity among the samples studied herein. These results can be preliminary explained as follows. Cu, Co, and Ni belong to a group of metals with low hydrogen overpotential and low catalytic activity towards the breaking of the N–B bond in AB. Additionally, these metals have strong adsorption affinity for hydrogen and ammonium species. Thus, during the catalytic hydrolysis of AB to hydrogen and ammonium, reaction intermediates may adsorb strongly on the surface of Cu, Co, and Ni, leading to a sluggish desorption of hydrogen. Since Cu has a lower overpotential for the hydrogen evolution reaction as compared to Ni and Co, this metal reacts readily with AB to adsorb hydrogen, while Ni and Co are less active. In the case of alloys, Cu and Ni (or Co) interact with each other, thereby weakening the adsorption

Table 2 – H_2 generation rate for the hydrolysis of AB catalyzed by 29.7 mg catalyst in 10 mL 0.5 wt % AB solutions at different temperatures.

Temperature (°C)	H_2 generation rate ($mL \cdot min^{-1} \cdot g^{-1}$) with different catalysts			
	$Co_{0.52}Cu_{0.48}$ prepared with starch	$Co_{0.52}Cu_{0.48}$ prepared without starch	$Ni_{0.19}Cu_{0.81}$ prepared with starch	$Ni_{0.19}Cu_{0.81}$ prepared without starch
20 ± 2	1212	370	1313	539
25 ± 2	1583	640	1684	875
30 ± 2	2020	872	2155	1111
35 ± 2	2458	976	2492	1380

Table 3 – Catalytic activity of different catalysts used for the hydrolytic dehydrogenation of AB or $NaBH_4$.

Catalys	TOF (mol H_2.mol^{-1} Catalyst·min^{-1})		E_a ($KJ \cdot mol^{-1}$)		Hydrogen generation rates (mL H2)/(catalyst·min-1)		Re-usability (Retained rate after 5 cycles)	Ref.
	AB	$NaBH_4$	AB	NaBH4	AB	$NaBH_4$	AB	
Ru@Ni/graphene	339.5	–	36.59	–	–	–	87%	[36]
$Ni_{91}P_9$/rGo	13.3	–	34.7	–	–	–	–	[37]
Ag@CoFe/graphene	82.9	–	32.79	–	–	–	59%	[34]
$Co_{0.9}Ni_{0.1}$/graphene	16.4	–	13.49	–	–	–	44%	[35]
p (AMPS)-Co:Ni	49		33.5				79%	[38]
RhNi@ZIF-8	58.8	–		–	–	–	–	[39]
P (4-vp)-Co	2.8	–	34.98	28.75	–	882	–	[40]
P(HEMA)-Co	–		–	37.01	–	1596	–	[41]
P (2vp-co-4-vp)	–	–	–	46.44	–	–	–	[42]
Pt_3Co	–	–	–	–	1380	–	–	[31]
Pt_3Ni	–	–	–	–	1388	–	–	[31]
cap-p (VI)-Co	–	–	51.58	41.46	–	–	–	[43]
$Co_{0.52}Cu_{0.48}$	3.4	–	33.7	–	2179	–	66%	this work
$Ni_{0.19}Cu_{0.81}$	2.7	–	33.3		2066		61%	this work

Table 4 – Reticular density calculation for the as-prepaed alloys (Each ball represents 52% Co and 48% Cu (or 19% Ni and 81% Cu)).

Crystalline plane	Crystal structure	Side view	Reticular density
{200}	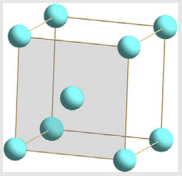	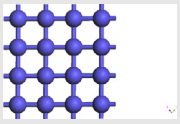	$\frac{\sqrt{36}}{3}$
{220}	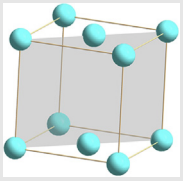	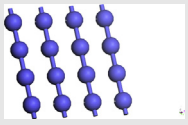	$\frac{\sqrt{18}}{3}$
{111}	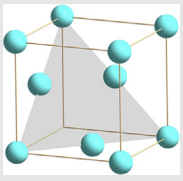	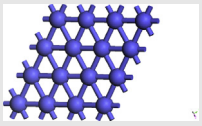	$\frac{\sqrt{48}}{3}$

of hydrogen and ammonium on the metal surface and leading to higher r values. Therefore, alloys are more efficient than pure Cu, Co, and Ni metals in catalyzing the hydrolysis reaction.

The crystal structures, the atomic arrangements perpendicular to the three crystalline planes, and the reticular density of the $Co_{0.52}Cu_{0.48}$ and $Ni_{0.19}Cu_{0.81}$ alloys are shown in Table 4. $Co_{0.52}Cu_{0.48}$ and $Ni_{0.19}Cu_{0.81}$ alloys both showed a fcc structure with each ion located on a separate, interpenetrating fcc lattice [44]. The calculated reticular density order for the non-interpenetrating fcc structure was {111} > {100} > {110}. Without differentiating the Cu and Co (Ni) atoms in the atomic arrangement, the reticular density order for the alloy was {100} > {110} > {111} as a result of interpenetration of the two separated fcc elements. On the basis of this calculation, the {111} faces would have the lowest surface energy, while the {111} planes would be the most favorable catalytic surface. In the starch solution, the {111} planes were atom-terminated while avoiding the direct exposition of planes to the oxygen-rich environment and minimizing the overall energy [45]. An approximation suggested that the {220} surfaces possess coordinately unsaturated alloy atoms, in which each two alloy atoms have a dangling bond. Bearing this in mind, the following surface energy order could be deduced: {220}> {200} > {111}. The {111} planes are saturated and has a lower surface energy, thereby stabilizing the alloy atoms. The XRD (Fig. 1) and SEAD (Fig. 4c and f) results revealed that the alloy is more likely to form {111} planes. These {111} planes have low surface energy and high reticular density, and no unsaturated bonds are present in these planes. Thus, a higher number of active sites is present in these planes, thereby improving the contact of the alloy with AB and increasing the amount of hydrogen released results .

Conclusions

In summary, $Co_{0.52}Cu_{0.48}$ and $Ni_{0.19}Cu_{0.81}$ alloys with dendritic branches of ca. 200–500 nm in length were prepared with starch. Cross-linked dendritic alloys with particle diameters of ca. 5 nm were synthesized by an in situ method. The as-prepared $Co_{0.52}Cu_{0.48}$ and $Ni_{0.19}Cu_{0.81}$ alloys were investigated as hydrogen generation catalysts via AB hydrolysis. The results showed that the as-synthesized $Co_{0.52}Cu_{0.48}$ and $Ni_{0.19}Cu_{0.81}$ alloys outperformed pure metal (Cu, Co, or Ni) catalysts and showed higher r values. The $Co_{0.52}Cu_{0.48}$ and $Ni_{0.19}Cu_{0.81}$ alloys catalysts showed good performance in terms of r, hydrogen generation efficiency, and apparent E_a. Molecular modelling calculations of the alloys revealed the {111} planes to have low surface energy, high large reticular density, and no unsaturated bonds. Thus, the higher number of active sites allowed to enhance the alloy–AB contact, thereby increasing the hydrogen production from AB in short times. This system consisting of AB and $Co_{0.52}Cu_{0.48}$ and $Ni_{0.19}Cu_{0.81}$ alloy NPs prepared with starch may finds applications in the field of on-board hydrogen supply.

Acknowledgments

This work was supported by the National Natural Science Foundation of China (No. 51301057, 21603052, 51401074, and 51272064), Natural Science Foundation of Hebei Province (No. B2015202346), Natural Science Foundation of Tianjin City of China (15JCYBJC47100).

REFERENCES

[1] Yang XJ, L LL, Sang WL, Zhao JL, Wang XX, Yu C, et al. Boron nitride supported Ni nanoparticles as catalysts for hydrogen generation from hydrolysis of ammonia borane. J Alloy Compd 2017;693:642–9.
[2] Zhong WD, Tian XK, Yang C, Zhou ZX, Liu XW, Li Y. Active 3D Pd/graphene aerogel catalyst for hydrogen generation from the hydrolysis of ammonia–borane. Int J Hydrogen Energy 2016;41(34):15225–35.
[3] Yurderi M, Bulu A, Zahmakiran M. Supported copper–copper oxide nanoparticles as active, stable and low–cost catalyst in the methanolysis of ammonia–borane for chemical hydrogen storage. Appl Catal B-Environ 2015;165(6):169–75.
[4] Zhou QX, Yang HX, Xu CX. Nanoporous Ru as highly efficient catalyst for hydrolysis of ammonia borane. Int J Hydrogen Energy 2016;41(30):12714–21.
[5] Yang XJ, Cheng FY, Liang J, Tao ZL, Chen J. Pt_xNi_{1-x} nanoparticles as catalysts for hydrogen generation from hydrolysis of ammonia borane. Int J Hydrogen Energy 2009;34(21):8785–91.
[6] Yang XJ, Cheng FY, Tao ZL, Chen J. Hydrolytic dehydrogenation of ammonia borane catalyzed by carbon supported Co core–Pt shell nanoparticles. J Power Sources 2011;196(5):2785–9.
[7] Talbot MO, Pham TN. Investigation of ligand steric effect on the hydrogen gas produced via a nickel-catalyzed dehydrogenation of ammonia–borane utilizing unsymmetrical triazolylidene ligands. Polyhedron 2016;114:415–21.
[8] Tonbul Y, Akbayrak S, Özkar S. Palladium(0) nanoparticles supported on ceria: highly active and reusable catalyst in hydrogen generation from the hydrolysis of ammonia borane. Int J Hydrogen Energy 2016;41(26):11154–62.
[9] Perathoner S, Centi G, Su D. Turning perspective in photoelectrocatalytic cells for solar fuels. ChemSusChem 2016;9(4):345–57.
[10] Zhang L, Zhou LQ, Yang KZ, Gao DD, Huang C. Pd–Ni nanoparticles supported on MIL–101 as high–performance catalysts for hydrogen generation from ammonia borane. J Alloy Compd 2016;677:87–95.
[11] Yang XJ, Cheng FY, Liang J, Tao ZL, Chen J. Carbon-supported $Ni_{1-x}@Pt_x$ (x= 0.32, 0.43, 0.60, 0.67, and 0.80) core–shell nanoparticles as catalysts for hydrogen generation from hydrolysis of ammonia borane. Int J Hydrogen Energy 2011;36(3):1984–90.
[12] Xu W, Li Q, Huang M. Design and analysis of liquid hydrogen storage tank for high–altitude long–endurance remotely–operated aircraft. Int J Hydrogen Energy 2015;40(46):16578–86.
[13] Ke D, Li Y, Wang J, Zhang L. Facile fabrication of poly(amidoamine) (PAMAM) dendrimers–encapsulated Ag–Co bimetallic nanoparticles for highly efficient dehydrogenation of ammonia borane. Int J Hydrogen Energy 2016;41(4):2564–74.
[14] Yang L, Luo W, Cheng GZ. Graphene-supported Ag-Based core-shell nanoparticles for hydrogen generation in hydrolysis of ammonia borane and methylamine borane. ACS AMI 2013;8:8231–40.
[15] Metin Ö, Özkar S. Monodisperse nickel nanoparticles supported on SiO_2 as an effective catalyst for the hydrolysis of ammonia–borane. Nano Res 2010;3(9):676–84.
[16] Liao JY, Li H, Zhang XB. Preparation of Ti supported Co film composed of Co nanofibers as catalyst for the hydrolysis of ammonia borane. Catal Commun 2015;67:1–5.
[17] Wang HX, Zhou LM, Han M, Tao ZL, Cheng FY, Chen J. CuCo nanoparticles supported on hierarchically porous carbon as catalysts for hydrolysis of ammonia borane. J Alloy Compd 2015;651:382–8.
[18] Ozay O, Inger E, Aktas N, Sahiner N. Hydrogen production from ammonia borane via hydrogel template synthesized Cu, Ni, Co composites. Int J Hydrogen Energy 2011;36(14):8209–82164.
[19] Song FZ, Zhu QL, Yang XC, Xu Q. Monodispersed CuCo nanoparticles supported on diamine-functionalized graphene as a non–noble metal catalyst for hydrolytic dehydrogenation of ammonia borane. Chemnanomat 2016;2(10):942–5.
[20] Lu ZH, Li JP, Feng G, Yao QL, Zhang F, Zhou RY, et al. Synergistic catalysis of MCM–41 immobilized Cu–Ni nanoparticles in hydrolytic dehydrogeneration of ammonia borane. Int J Hydrogen Energy 2014;39(25):13389–95.
[21] Zhang J, Li HB, Zhang H, Zhu YM, Mi G. Porously hierarchical Cu@Ni cubic–cage microstructure: very active and durable catalyst for hydrolytically liberating H2 gas from ammonia borane. Renew Energy 2016;99:1038–45.
[22] Zhang H, Chen CC, An CH, Xu YA, Huang YA. Facile synthesis of Cu@CoNi core–shell nanoparticles composites for the catalytic hydrolysis of ammonia borane. Int J Hydrogen Energy 2015;40(36):12253–61.
[23] Sharma B, Gujral HS, Solah V. Effect of incorporating finger millet in wheat flour on mixolab behavior, chapatti quality and starch digestibility. Food Chem 2017;231:156–64.
[24] Yan JM, Zhang XB, Han S, Shioyama H, Xu Q. Synthesis of longtime water/air-stable Ni nanoparticles and their high catalytic activity for hydrolysis of ammonia-borane for hydrogen generation. Inorg Chem 2009;48:7389–93.
[25] Liang HY, Chen GZ, Desinan S, Rosei R, Rosei F, Ma Dl. In situ facile synthesis of ruthenium nanocluster catalyst supported on carbon black for hydrogen generation from the hydrolysis of ammonia-borane. Int J Hydrogen Energy 2012;37:17921–7.
[26] Zhao JZ, Ma H, Chen J. Improved hydrogen generation from alkaline $NaBH_4$ solution using carbon-supported Co–B as catalysts. Int J Hydrogen Energy 2007;32(18):4711–6.
[27] Rakap M, Kalu EE, Özkar S. Hydrogen generation from the hydrolysis of ammonia borane using cobalt–nickel–phosphorus (Co–Ni–P) catalyst supported on Pd–activated TiO_2 by electroless deposition. Int J Hydrogen Energy 2011;36(1):254–61.
[28] Eom KS, Cho KW, Kwon HS. Hydrogen generation from hydrolysis of NH_3BH_3 by an electroplated Co–P catalyst. Int J Hydrogen Energy 2010;35(1):181–6.
[29] Yang L, Su J, Meng X, Lu W, Cheng G. In situ synthesis of graphene supported Ag@CoNi core–shell nanoparticles as highly efficient catalysts for hydrogen generation from hydrolysis of ammonia borane and methylamine borane. J Mater Chem A 2013;1(34):10016–23.
[30] Yu C, Li XP, Liu ZY, Yang XJ, Huang Y, Lin J, et al. Synthesis of hierarchically porous TiO_2 nanomaterials using alginate as soft templates. Mater Res Bull 2016;83:609–14.
[31] Yao CF, Zhuang L, Cao YL, Ai XP, Yang HX. Hydrogen release from hydrolysis of borazane on Pt- and Ni-based alloy catalysts. Int J Hydrogen Energy 2008;33(10):2462–7.

[32] Li C, Zhou J, Gao W, Zhao J, Liu J, Zhao Y, et al. Binary Cu–Co catalysts derived from hydrotalcites with excellent activity and recyclability towards NH_3BH_3 dehydrogenation. J Mater Chem A 2013;1(17):5370–6.
[33] Yamada Y, Yano K, Xu Q, Fukuzumi S. Cu/Co_3O_4 nanoparticles as catalysts for hydrogen evolution from ammonia borane by hydrolysis. J Phys Chem C 2010;114(39):16456–62.
[34] Yang L, Su J, Luo W, Cheng GZ. Strategic synthesis of graphene supported trimetallic Ag-based core-shell nanoparticles toward hydrolytic dehydrogenation of amine boranes. Int J Hydrogen Energy 2014;39:3360–70.
[35] Feng WQ, Yang L, Cao N, Du C, Dai HG, Luo W, et al. In situ facile synthesis of bimetallic CoNi catalyst supported on graphene for hydrolytic dehydrogenation of amine borane. Int J Hydrogen Energy 2014;39:3371–80.
[36] Cao N, Su J, Luo W, Cheng GZ. Hydrolytic dehydrogenation of ammonia borane and methylamine borane catalyzed by graphene supported Ru@Ni core-shell nanoparticles. Int J Hydrogen Energy 2014;39:426–35.
[37] Du XQ, Yang CL, Zeng X, Wu T, Zhou YH, Cai P, et al. Amorphous NiP supported on rGO for superior hydrogen generation from hydrolysis of ammonia borane. Int J Hydrogen Energy 2017;42:14181–7.
[38] Nurettin S, Ozgur O, Nahit A, Erk I, Jibao H. The on demand generation of hydrogen from Co-Ni bimetallic nano catalyst prepared by dual use of hydrogel: as template and as reactor. Int J Hydrogen Energy 2011;36:15250–8.
[39] Xia BQ, Liu C, Wu H, Luo W, Cheng GZ. Hydrolytic dehydrogenation of ammonia borane catalyzed by metal-organic framework supported bimetallic RhNi nanoparticles. Int J Hydrogen Energy 2015;40:16391–7.
[40] Nurettin S, Sema Y. Preparation of superporous poly(4-vinyl pyridine) cryogel and their templated metal nanoparticle composites for H_2 production via hydrolysis reactions. Fuel Process Technol 2014;126:324–31.
[41] Fahriye S, Nurettin S. Superporous P(2-hydroxyethyl methacrylate) cryogel-M (M: Co, Ni, Cu) composites as highly effective catalysts in H_2 generation from hydrolysis of $NaBH_4$ and NH_3BH_3. Int J Hydrogen Energy 2014;39:15455–63.
[42] Nurettin S, Alper OY. Monodispersed p(2-VP) and p(2-VP-co-4-VP) particle preparation and their use as template for metal nanoparticle and as catalyst for H2 production from $NaBH_4$ and NH_3BH_3 hydrolysis. Int J Hydrogen Energy 2014;39:10476–84.
[43] Nurettin S, Alper OY. H_2 generation from $NaBH_4$ and NH_3BH_3 using metal catalysts prepared within p(VI) capsule particles. Fuel Process Technol 2014;125:148–54.
[44] Peng ZP, Jiang YS, Song YH, Wang C, Zhang HJ. Morphology control of nanoscale PbS particles in a polyol process. Chem Mater 2008;20(9):3153–62.
[45] Leng M, Yu C, Wang C. Polyhedral Cu_2O particles: shape evolution and catalytic activity on crosscoupling reaction of iodobenzene and phenol. CrystEngComm 2012;14(24):8454–61.